The pathophysiological mechanism of kidney injury caused by *Beni-koji Choleste-Help*/puberulic acid is proximal tubular mitochondrial dysfunction

Yuta Sekiguchi[1], Makiko Mori[1], Haruka Maruyama[1,2], Yuki Nakao[1], Hiroaki Kikuchi[1], Shintaro Mandai[1], Fumiaki Ando[1], Koichiro Susa[1], Takayasu Mori[1], Yuma Waseda[3], Soichiro Yoshida[3], Yasuhisa Fujii[3], Wakana Shoda[4], Daiei Takahashi[4], Eisei Sohara[1], Shinichi Uchida[1], Yutaro Mori[1]

[1]Department of Nephrology and [3]Department of Urology, Graduate School of Medical and Dental Sciences, Institute of Science Tokyo, Tokyo 113-8510, Japan.

[2]Kidney Disease and Transplant Center, Shonan Kamakura General Hospital, Kamakura 247-8533, Japan

[4]Department of Nephrology, Japanese Red Cross Musashino Hospital, Tokyo 180-0023, Japan.

Lead contact and Corresponding author:

Yutaro Mori, MD, PhD

Department of Nephrology

Graduate School of Medical and Dental Sciences

Institute of Science Tokyo

1-5-45, Yushima, Bunkyo-ku, Tokyo 113-8510, Japan

Phone: +81-3-5803-5214; Fax: +81-3-5803-5215; Email: y-mori.kid@tmd.ac.jp

Abstract

In March 2024, kidney injury sometimes accompanied with Fanconi syndrome caused by a supplement made from red yeast rice (*Beni-koji Choleste-Help*) were reported in Japan. By November 24, 2024, 2,628 people had visited medical facilities, resulting in a social problem. Many patients still have a decline in eGFR. The previous report, however, did not indicate anything other than that puberulic acid which newly identified nephrotoxicity was contained in toxic lots. The pathophysiology of those nephropathies should be determined. Here, we discovered that mitochondrial dysfunction in renal proximal tubular epithelial cells plays a pivotal role in them. A patient renal biopsy sample showed Kidney Injury Molecule-1 (KIM-1) expression in proximal tubules surrounded by activated myofibroblasts, indicating acute tubular damage and interstitial fibrosis associated with injured tubules. Mice treated with the toxic lot of *Choleste-Help* and puberulic acid showed kidney injury with Fanconi syndrome-like urinary findings. Pathological sections showed tubular necrosis and interstitial fibrosis. RNA-seq on whole kidneys of those mice presented the renal damage caused by *Choleste-Help* and puberulic acid produced similar RNA patterns, indicating puberulic acid is a causative agent. Gene Ontology (GO) analysis comparing the normal and toxic lot revealed downregulation of mitochondrial-related pathways. Puberulic acid also showed toxicity on human primary epithelial cells and tubular organoids. *In vitro* experiments with human primary cells revealed that it causes mitochondrial damage at first and leads to cell death, mainly necrosis. Thus, puberulic and a toxic lot of *Choleste-Help* cause direct mitochondrial damage on tubular epithelial cells, followed by necrosis.

Keywords

Acute kidney injury, organoid, tubuloid, puberulic acid, Fanconi syndrome

43 **Graphical Abstract**

44

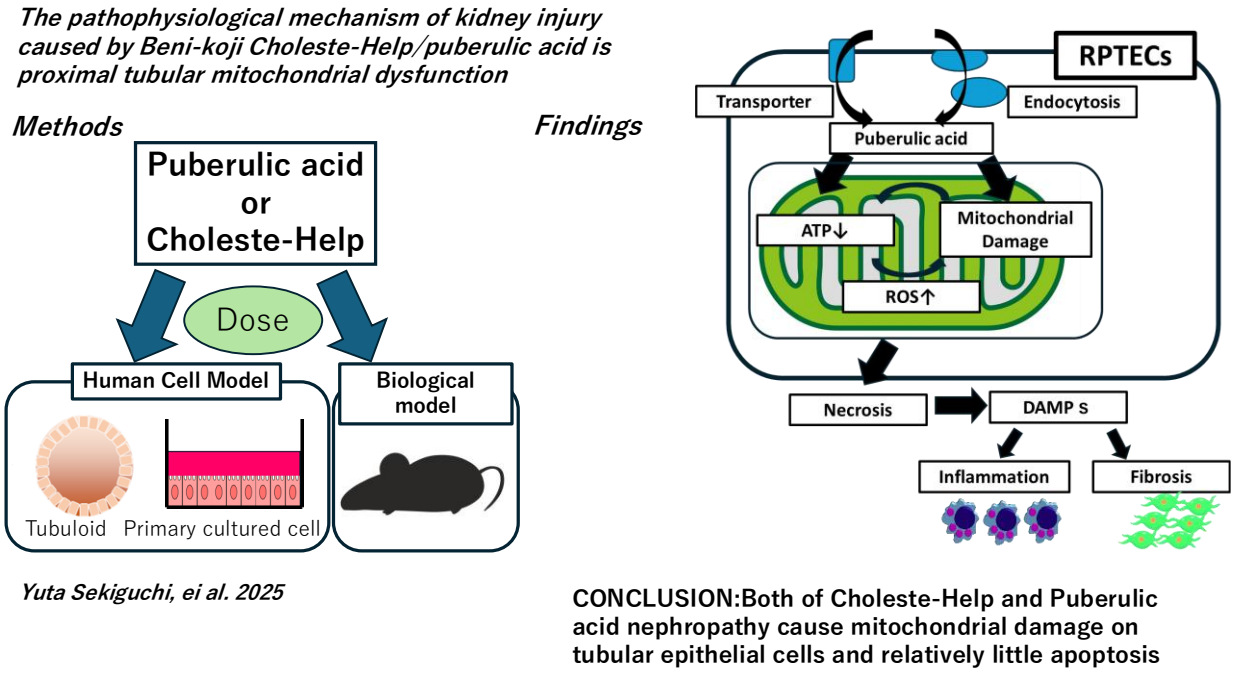

45

46

47 **Translational Statement**

48 Our research revealed the pathophysiology of puberilic acid nephropathy, which suffers many

49 patients. And we used not only animal models, but human kidney-derived primary cultured tubular

50 epithelial cells and its 3D organoids, which are ones of the closest models of human body.

51

52 **Introduction**

53 In recent years, due to growing health consciousness, supplements and herbal medicines are widely
54 used. However, these often produce side effects.[1,2] From the second half of 2023 to 2024, a serious
55 health issue arose in Japan. Multiple cases of kidney dysfunction associated with Benikoji tablets
56 were reported, prompting Kobayashi Pharmaceutical Co., Ltd. to implement a voluntary recall on
57 March 22, 2024.[3] The supplement most taken by patients was *Beni-koji Choleste-Help（Choleste-*
58 *Help）*. This supplement, which contains Monascus-derived red yeast[4] and a compound structurally
59 similar to the cholesterol-lowering drug lovastatin, was marketed as achieving similar effects at
60 lower concentrations.[5] Patients who took these supplements developed acute kidney injury,
61 proteinuria, and Fanconi syndrome[6-8], and many patients still had CKD-level kidney damage 120
62 days after starting treatment.[9] A compound called puberulic acid and two other new compounds
63 were identified as causative substances, and puberulic acid is the most likely causative
64 substance[10,11], but only little information[12,13] are available at this time. Puberulic acid was
65 originally developed as an antimalarial agent; however, its development was discontinued due to
66 lethality observed in mice at high doses, the cause of which remains unknown.[14] Aristolochic acid,
67 the most widely known kidney-toxic substance derived from traditional Chinese medicine, is
68 known not only to cause tubular damage, but also to induce CKD and increase the incidence of
69 cancer[15-17]. Therefore, it is necessary to collect various information on this substance, including its
70 damaged pathways and clinical course. We have succeeded in identifying the main pathways of
71 damage to the kidneys caused by this substance from a basic medical perspective, and we describe
72 this in this paper. To the best of our knowledge, this is the first study to demonstrate the toxicity
73 of puberulic acid in human cells.

Methods

Immunostaining of human renal biopsy samples

Written informed consent was obtained by the patient of *Choleste-Help* nephropathy for publishing reports regarding renal biopsy and other clinical information. After deparaffinization with xylene, antigen retrieval was performed by heat-induced epitope retrieval using boiling in Antigen Unmasking Solution (Citric Acid base, H-3300, Vector Laboratories Inc.). Sections were incubated with a goat anti-KIM-1 antibody (1:200, AF1750, R&D Systems, MN, USA) and a rabbit anti-α-smooth muscle actin (α-SMA) antibody conjugated with Cy3 (1:400, C6198, Sigma-Aldrich). For the detection of KIM-1, an Alexa Fluor 488-conjugated donkey anti-goat IgG secondary antibody (1:500, A11055 Thermo Fisher Scientific) was used.

Animal treatment and tissue collection

Eight-week-old male C57BL/6J mice were used for all experiments. Mice were randomly assigned to four groups (n = 6-10 per group): (1) control (PBS), (2) *Choleste-Help* normal batch (1,000 mg/day), (3) *Choleste-Help* toxic batch (1,000 mg/day), and (4) puberulic acid (1 mg/day). Treatments were administered either by oral gavage or intraperitoneal injection for six consecutive days, followed by a one-day rest period. On day 7, mice were euthanized, and bloods, urines, and whole kidneys were rapidly harvested, snap-frozen in liquid nitrogen, and stored at −80°C until RNA extraction. Hematological and urinary analyses were outsourced and performed by Oriental Yeast Co., Ltd.

Histological Preparation and Staining

97 Hematoxylin and eosin (H&E) staining was outsourced to the Research Core Center of Institute of
98 Science Tokyo. Masson's trichrome staining was performed using a standard protocol. For each
99 sample, one kidney sections were selected to reduce non-specific blue staining. Whole images of
100 the sections were acquired, and the fibrotic area, indicated by blue staining, was quantified using
101 Image J Fiji (https://imagej.net/software/fiji/downloads). The percentage of the blue-stained area
102 relative to the total kidney section area was calculated for each sample.
103
104 **RNA-seq and analysis**
105 Mouse whole kidney total RNA was extracted using Sepasol (Nacalai Tesque, Japan) and purified
106 with Direct-zol RNA Miniprep Plus Kit (Zymo Research, R2070). Samples (n = 5, each) with RIN
107 > 7.5 were processed by ReRexa Inc. using NEBNext kits and sequenced on NovaSeq X Plus (2
108 × 150 bp, ~ 40 million reads/sample). Reads were trimmed with fastp and quantified with Salmon
109 (GENCODE vM33). DEGs were identified using DESeq2 (padj < 0.05, |log2FC| > 1, baseMean >
110 10). PCA and heatmaps were generated in RStudio (Windows), with Salmon outputs from WSL2.
111 The details of experimental methods for RNA-seq analysis are described in **Supplementary**
112 **Methods**.
113
114 **Cell culture experiment**
115 Human kidney samples were collected from patients undergoing clinically indicated nephrectomy
116 at the Institute of Science Tokyo Hospital in Tokyo, Japan. The protocol was approved by the
117 Institutional Review Board of the Ethics Committee of Institute of Science Tokyo (M2022-005).
118 Primary human renal proximal tubular epithelial cells (hRPTECs) were isolated from unaffected
119 areas of kidneys removed during nephrectomy procedures performed on patients with renal cell

120 carcinoma or urinary tract malignancies by modifying a previously established protocol.[18,19]
121 Briefly, the isolation procedure involved mincing the human renal cortex and then digesting it in
122 a solution of Collagenase type II (1.0 mg/mL) (Worthington Biochemical, NJ, USA). The enzyme
123 reaction was terminated with fetal bovine serum (FBS), and the samples were resuspended in
124 hRPTECs culture medium containing DMEM/F-12 (Nacalai Tesque, Kyoto, Japan), with BSA
125 (Nacalai Tesque), Antibiotic–Antimycotic (ThermoFisher Scientific, MA, USA), hydrocortisone
126 (ThermoFisher Scientific, MA, USA), ITS liquid media supplement (Sigma-Aldrich, MO, USA),
127 and human recombinant epidermal growth factor (EGF) (ThermoFisher Scientific, MA, USA).
128
129 **Human renal tubuloids culture**
130 hRPTECs were seeded onto ultralow attachment plates at a density of 5.0×10^5 cells/well using
131 Advanced RPMI 1640 medium (ThermoFisher Scientific), supplemented with 5% FBS. After a 2–
132 3-day incubation period, Matrigel (Corning, NY, USA) was added to stimulate tubuloid formation.
133 The following day, the culture medium was changed to Advanced RPMI 1640 medium with 5%
134 FBS, EGF, FGF2, and HGF (tubuloids media). Media was changed three times in a week to
135 maintain optimal cell growth conditions. Tubuloids were usually ready for experimentation within
136 1–2 weeks of starting the culture.
137
138 **Western blot analysis**
139 The samples were lysed, and the protein was purified by using a lysis buffer [50 mM Tris-HCl (pH
140 7.5), 150 mM NaCl, 1% Nonidet P-40, 1 mM sodium orthovanadate, 50 mM sodium fluoride, and
141 protease inhibitor cocktail]. Since the protein content of the Tuburoids was low, four wells under
142 the same conditions were combined into a single sample. Proteins were separated by 10% SDS-

143 PAGE and transferred onto a nitrocellulose membrane. Protein bands were visualized using
144 Western Blue (Promega, WI, USA). Rabbit anti–ERK1/2 (p44/42 MAPK) antibody (9102S, Cell
145 Signaling Technology) (1:1000) or rabbit anti-beta actin antibody (4967S, Cell Signaling
146 Technology) (1:1000) was used as a loading control. Primary antibodies were also used, such as
147 rabbit anti-KIM-1 polyclonal antibody (PA5-79345, Thermo Fisher Scientific) (1:1000), rabbit
148 anti Phospho-Histone H2AX (Ser139) antibody (9718S, Cell Signaling Technology) (1:1000). As
149 secondary antibody**,** anti-rabbit IgG alkaline phosphatase–conjugated secondary antibody (S373B,
150 Promega) was used. Densitometry was performed by using Image J Fiji.
151
152 **Cell viability assay**
153 Primary cultured cells were seeded at a density of 2×10^4 cells per well in 96-well plates. After
154 reaching confluence in two days post-passaging, cells were treated with the indicated compound
155 for 48 hours. Cell viability was assessed using Cell Count Reagent SF (Nacalai Tesque, #07553)
156 according to the manufacturer's instructions. Cells were incubated with the reagent (10% v/v) at
157 37 °C for 1 hour. Absorbance was measured at 450 nm using a microplate reader (FilterMax F5,
158 Molecular Devices). Cell viability was expressed as a percentage of absorbance relative to vehicle
159 control. The EC_{50} value was estimated using a four-parameter logistic model fitted to the viability
160 data. Due to data sparsity at higher concentrations, the confidence intervals could not be fully
161 resolved. Therefore, the EC_{50} value should be interpreted with caution.
162
163 **Annexin V assay and flow cytometry**
164 Primary cultured cells were seeded at a density of 5×10^5 cells per well in 12-well plates. After
165 reaching confluence in two days post-passaging, cells were treated with the indicated compound

166 for 48 hours. Following treatment, 1×10^5 cells were collected and stained using the Annexin V
167 Apoptosis Detection Kit (Nacalai Tesque, product number 15342-54) according to the
168 manufacturer's instructions. Flow cytometric analysis was performed using a FACS Lyric™
169 system (BD Biosciences). Data was analyzed with FlowJo software (BD Biosciences), and cell
170 populations were classified into live, early apoptotic, and late apoptotic/necrotic based on Annexin
171 V and propidium iodide (PI) staining patterns.
172
173 **JC-1 staining**
174 Primary cultured cells were seeded at a density of 5×10^5 cells per well in 12-well plates. In three
175 days post-passaging, cells were treated with the indicated compound for 18 or 24 hours. Then,
176 mitochondrial membrane potential was assessed using the JC-1 dye (T3168, Thermo Fisher
177 Scientific) according to the manufacturer's instructions. Briefly, cells were incubated with 1.5 μM
178 JC-1 in culture medium at 37 °C for 20 minutes. After incubation, cells were washed twice with
179 PBS and analyzed by confocal microscopy (Eclipse Ti2 from Nikon, excitation/emission:
180 488/530 nm for green monomers, 540/590 nm for red aggregates), with the NIS-Elements
181 Advanced Research microscope system serving as the operating system. Fluorescence images
182 were analyzed using ImageJ Fiji. For each well, three fields of view were randomly selected, and
183 the entire field area was defined as the region of interest (ROI). The red-to-green fluorescence ratio
184 was calculated to assess mitochondrial membrane potential.
185
186 **ATP measurement**
187 Primary cultured cells were seeded at a density of 2×10^4 cells per well in 96-well plates. After
188 reaching confluence in two days post-passaging, cells were treated with the indicated compound

189 for 6, 24 or 48 hours. Cellular ATP levels were quantified using the CellTiter-Glo® 2.0 Cell
190 Viability Assay (Promega, Madison, WI, USA) according to the manufacturer's instructions.
191 Luminescence was measured using a Varioskan™ LUX Multimode Microplate Reader (Thermo
192 Fisher Scientific, Waltham, MA, USA). The luminescence intensity, which is proportional to the
193 amount of ATP, was recorded and normalized to control samples.
194
195 **Quantification and statistical analyses**
196 Figure Legends indicate the number of samples assayed in each experiment. One-way ANOVA
197 was used for general comparisons. When data were normalized to the control group mean, Welch's
198 ANOVA was applied. When each value was individually normalized to its corresponding control,
199 the Kruskal–Wallis test was used. A p-value < 0.05 was considered statistically significant.
200 Statistical significance was indicated by asterisks as follows: * $p < 0.05$, ** $p < 0.01$, *** $p < 0.001$,
201 **** $p < 0.0001$. All statistical analyses were performed with GraphPad Prism by GraphPad
202 Software Inc. (San Diego, CA, USA).
203
204 **Study approval**
205 The protocol for human kidney samples for primary culture and the one for analyzing human
206 kidney biopsy samples were approved by the Institutional Review Board of the Ethics Committee
207 of Institute of Science Tokyo (M2022-005, I2024-097). Animal experiments were approved by the
208 Animal Care and Use Committee of Institute of Science Tokyo (A2023-109C3) according to the
209 animal experiment guidelines of the Japan Ministry of Education, Culture, Sports, Science and
210 Technology.
211

212 **Results**

213 **A human kidney biopsy sample of a *Choleste-Help* patient show KIM-1 positive proximal**
214 **tubular epithelial cells surrounded by α-SMA positive cells**

215 Renal biopsy samples obtained from a patient who visited our affiliated hospital revealed marked
216 tubular dilatation and detachment of tubular epithelial cells and tubular casts were observed in the
217 lumen of the renal tubules (**Figure 1a**), whose case we reported recently.[7] Immunostaining
218 demonstrated the presence of KIM-1–positive tubular epithelial cells, an established marker of
219 tubular injury,[20] along with surrounding expression of α-SMA, indicative of early fibrotic changes
220 associated with tubular epithelial damage (**Figure 1b**). Although the degree of renal injury in this
221 case was relatively mild, the findings suggest the presence of fibrosis at an early stage.

222

223 **Wild type mice showed acute kidney failure and Fanconi-like phenotype by *Choleste-Help***
224 **toxic lot and puberulic acid**

225 To investigate the *in vivo* toxicity and underlying mechanisms, we administered *Choleste-Help*
226 (normal lot and toxic lot), the suspected causative compound puberulic acid, and vehicle (PBS) to
227 mice once daily for six days. Following a one-day drug holiday, the mice were sacrificed on day
228 7 (**Figure 2a, Supplementary Figure 1**).

229 In both the *Choleste-Help* toxic lot and puberulic acid groups, serum biochemical analysis
230 revealed elevated blood urea nitrogen (BUN) and creatinine (Cr) levels (**Figure 2b**). Urinalysis
231 showed increased urinary albumin-to-creatinine (Alb/Cr), glucose-to-creatinine (Glu/Cr), and N-
232 acetyl-β-D-glucosaminidase-to-creatinine (NAG/Cr) ratios, which is consistent not only with
233 tubular injury but also with Fanconi syndrome. These findings indicate that both compounds

234 induce proximal tubular injury, renal dysfunction, proteinuria, and a Fanconi syndrome-like
235 phenotype in mice, recapitulating features observed in human cases.

236 Histological examination using hematoxylin and eosin (HE) staining revealed tubular
237 dilatation and epithelial cell detachment (**Figure 2c**), consistent with human biopsy findings. In
238 addition, intratubular casts—also observed in human sample—were present in treated mice.
239 Furthermore, Masson's Trichrome staining demonstrated a significant increase in fibrotic areas in
240 both the *Choleste-Help* toxic lot and puberulic acid groups (**Figure 2d**). These results suggest that
241 *Choleste-Help* toxic lot and puberulic acid can induce renal fibrosis at an early stage *in vivo*.

242

243 **Mice treated with *Choleste-Help* toxic lot and puberulic acid exhibited highly similar gene**
244 **expression profiles, as revealed by RNA-seq analysis**

245 We performed bulk RNA sequencing (RNA-seq) using whole-kidney samples (n = 5 for each
246 sample) from the experimental groups as a transcriptomic analysis. Principal component analysis
247 (PCA) and hierarchical clustering (**Figure 3a, b**) demonstrated that the *Choleste-Help* toxic lot
248 and puberulic acid groups clustered closely together, indicating a high degree of similarity in their
249 transcriptomic responses.

250 To assess the overall transcriptomic changes and data quality, a volcano plot, generated to
251 compare gene expression between toxic lot vs normal lot and, and heatmap were generated (**Figure**
252 **3c, d, Supplementary Figure 2**). These visualizations illustrate the global expression landscape
253 and support the reliability and robustness of the dataset. In the Volcano plot, Spp1 and Havcr1
254 were among the top upregulated genes, supporting the validity of the model as a representation of
255 kidney injury.

256 Correlation analysis between differential gene expression profiles revealed a strong
257 correlation (Pearson's r = 0.736) between the comparisons of *Choleste-Help* toxic lot vs. normal
258 lot and puberulic acid vs. PBS (**Figure 3e**). Moreover, more than 70% of differentially expressed
259 genes (DEGs) overlapped between the two comparisons, suggesting that the toxic responses
260 induced by *Choleste-Help* toxic lot and puberulic acid are highly similar at the transcriptomic level
261 (**Figure 3f**).
262 Although the precise concentration of puberulic acid contained in *Choleste-Help* is
263 unknown and not equivalent to the dose used in the isolated puberulic acid group, the similarity in
264 gene expression patterns strongly suggests that puberulic acid is likely a major contributor to the
265 nephrotoxicity observed in *Choleste-Help* toxic lot.
266
267 **Mitochondrial function was significantly suppressed indicated by comprehensive**
268 **transcriptomic analysis with RNA-seq**
269 We performed Gene Ontology (GO) enrichment analysis based on the comparison between the
270 *Choleste-Help* toxic lot and the normal lot. Based on the GO cellular component (CC) analysis
271 using the absolute value of log2 fold change, the top 10 enriched terms included not only
272 membrane and cytoskeleton components but also mitochondria, indicating that mitochondrial
273 structures were among the most affected organelles (**Figure 4a**). Notably, all mitochondrial-related
274 terms showed a trend toward downregulation. Furthermore, in the GO biological process (BP)
275 analysis, the top 10 downregulated pathways were predominantly associated with mitochondrial
276 function (**Figure 4b**).

277 In addition, GO analysis of the "molecular function" category revealed downregulation of
278 various transporter activities, supporting the hypothesis that this compound induces a renal injury
279 pattern consistent with Fanconi syndrome (**Figure 4c**).
280
281 **Puberulic acid exhibited approximately half the cytotoxicity of cisplatin in hRPTECs and**
282 **kidney injury marker KIM-1 and DNA damage marker γH2AX were upregulated following**
283 **puberulic acid exposure**
284 To evaluate the potential nephrotoxicity of puberulic acid in humans, we exposed primary cultured
285 hRPTECs to puberulic acid for 48 hours and assessed cytotoxicity using a cell viability assay.
286 Cisplatin was included as a positive control under the same conditions. Puberulic acid exhibited
287 dose-dependent toxicity, with an EC_{50} of 61.78 μM, approximately twice that of cisplatin (EC_{50} =
288 32.27 μM), indicating moderate cytotoxicity relative to cisplatin (**Figure 5a**).
289 We further examined the effects of puberulic acid using both conventional 2D cultures and
290 3D-cultured renal tubuloids derived from hRPTECs. Puberulic acid was administered at 48-hour
291 intervals for a total of three exposures. Western blot analysis revealed increased expression of the
292 kidney injury marker KIM-1 in tubuloids and the DNA damage marker γH2AX in both models
293 following treatment (**Figure 5b, c**). Notably, the tubuloids responded to puberulic *acid* at
294 approximately one-tenth the concentration required in the 2D cultures, indicating higher sensitivity
295 in the 3D system.
296 DNA damage and its response are known to be associated with cellular senescence through
297 cell cycle arrest[21]. The senescence-associated secretory phenotype (SASP) is considered a driver
298 of chronic fibrosis progression.[22,23] In mouse RNA-seq data, Cdkn1a expression was markedly
299 upregulated, whereas Cdkn2a showed only a modest increase (**Supplementary Figure 3a**).

300 Furthermore, in the *in vitro* model with a 6-day exposure, no induction of p16 expression was
301 observed (**Supplementary Figure 3b**). These findings suggest that cell cycle arrest induced by
302 puberulic acid occurs without clear evidence of cellular senescence.
303
304 **Annexin V assay revealed that necrosis accounted for most of the cell death**
305 To evaluate the involvement of apoptosis, we performed live-cell immunostaining using Annexin
306 V and propidium iodide (PI), followed by flow cytometric analysis. As a positive control, cells
307 were treated with cisplatin, and the types of cell death were assessed at 48 hours post-treatment.
308 The results showed that, under conditions with comparable numbers of viable cells, the
309 proportion of apoptotic cells in the puberulic acid–treated group was approximately half that
310 observed in the cisplatin-treated group, indicating a relatively low level of apoptosis (**Figure 6a**).
311 Furthermore, at earlier points (24 and 40 hours), the proportion of apoptotic cells in the puberulic
312 acid group was even lower (**Figure 6b**).
313 These findings suggest that while puberulic acid does induce apoptosis, it occurs at
314 relatively low levels. This observation is consistent with the renal biopsy findings in human cases,
315 where necrosis was the predominant histological feature.
316 We also examined other forms of cell death, including necroptosis and pyroptosis
317 (**Supplementary Figure 4**); however, in our *in vitro* experiments, we did not observe upregulation
318 of pathway-specific molecules at the protein level, suggesting that necroptosis and pyroptosis are
319 not involved in puberulic acid-induced cell death.
320 In addition, at the 24-hour time point, exposure to 100 μM puberulic acid induced only
321 minimal cell death. Therefore, analyzing cells prior to this time point may provide further insights
322 into the upstream mechanisms responsible for puberulic acid–induced cytotoxicity.

323

324 **JC-1 staining and measuring of ATP revealed a decrease in mitochondrial membrane**
325 **potential and ATP depletion preceding the onset of cell death**

326 JC-1 staining was performed at 18- and 24-hours following treatment with 100 μM puberulic
327 acid—time points at which minimal cell death was observed (**Figure 7a**). At 18 hours, a reduction
328 in red fluorescence, indicative of healthy mitochondria, was already evident, accompanied by an
329 increase in green fluorescence, reflecting a loss of mitochondrial membrane potential. This trend
330 became more pronounced at 24 hours.

331 These findings indicate that mitochondrial dysfunction occurs prior to the onset of cell
332 death following puberulic acid exposure. Thus, puberulic acid–induced mitochondrial damage is
333 likely one of the primary causes of its cytotoxic effects.

334 In addition, ATP measurement using a luminescence-based assay revealed a reduction as
335 early as 6 hours after treatment (**Figure 7b**). This suggests that puberulic acid impairs ATP
336 production, likely through disruption of the mitochondrial respiratory chain.

337 **Discussion**

338 In this study, we have revealed potential pathophysiological mechanisms of puberulic acid or
339 *Choleste-Help* toxic lot-induced nephropathy. As reported by Ministry of Health, Labour and
340 Welfare in Japan, 1,961 people consulted with doctor and 348 people was hospitalized due to renal
341 injury after taking *Choleste-Help*.[3] The social significance of this study is extremely great.

342 We observed acute renal fibrosis in mouse models treated with puberulic acid or *Choleste-*
343 *Help* toxic lot as well as human patients. We also found out proximal tubular epithelial cell death
344 after puberulic acid treatment[7,9] in a relatively short period, which was mainly necrosis. In the
345 status of proximal tubular epithelial necrosis, Damage-Associated Molecular Patterns (DAMPs)
346 are released from dead cell bodies, resulting in myofibroblast activation and/or immune cell
347 infiltration.[24,25] This may explain the early onset of fibrosis observed in our model.

348 Mitochondrial damage was demonstrated by early reductions in ATP levels and JC-1
349 signals prior to cell death in hRPTECs, which was supported by RNA-seq data in mice treated
350 with pubeluric acid or *Choleste-Help* toxic lot. In addition, a marked reduction in mitochondria in
351 electron micrographs of kidneys from mice treated with puberulic acid was reported in a preprint,[12]
352 which is consistent with our findings. Since apoptosis is an ATP-dependent process,[26,27] it is well
353 known that necrosis tends to be predominant under conditions of ATP depletion.[28,29] Therefore,
354 we speculate that the primary mitochondrial damage led to a relative deficiency in ATP, which in
355 turn shifted the mode of cell death toward necrosis. Proximal tubular epithelial cells primarily
356 generate ATP through mitochondrial oxidative phosphorylation, relying heavily on β-oxidation of
357 fatty acids as an energy source, with minimal dependence on glycolysis. In the proximal tubule, a
358 significant portion of solute reabsorption occurs via secondary active transport driven by the
359 Na^+/K^+-ATPase, which requires a substantial amount of ATP.[30] When proximal tubular cells are

injured and mitochondrial dysfunction impairs energy production, ATP depletion ensues, resulting in characteristic features of Fanconi syndrome may emerge, including glucosuria, aminoaciduria, phosphaturia, bicarbonate loss leading to metabolic acidosis, and low molecular weight proteinuria.[31] This is highly consistent with the Fanconi syndrome-like manifestations observed in both humans and mice following treatment with puberulic acid and *Choleste-Help*. In the future, we plan to investigate the detailed mechanisms of puberulic acid, including its uptake pathways and long-term effects.

In summary, we are the first to demonstrate that puberulic acid and *Choleste-Help* exhibit the same type of toxicity, which is predominantly necrosis. We also showed that mitochondrial dysfunction precedes and likely contributes to this toxicity as one of its key mechanisms. We hope that future studies building on this work will contribute to improving the prognosis and treatment of patients suffering from such toxic effects.

372 **Disclosure Statement**

373 The authors declare that they have no conflicts of interest.

374

375 **Data Statement**

376 The data that support the findings of this study are available from the corresponding author upon
377 reasonable request. Requests for resources and reagents should be directed to the Lead Contact,
378 Yutaro Mori (y-mori.kid@tmd.ac.jp).

379

380 **Acknowledgment**

381 We are deeply grateful to the generous study participants who agreed to donate segments of their
382 resected kidneys for this research. This work was supported by Leading Initiative for Excellent
383 Young Researchers (LEADER) from Ministry of Education, Culture, Sports, Science and
384 Technology (to Y.M.), Grant-in-Aid for Research Activity Start-up (22K20881) and Grand-in-Aid
385 for Scientific Research (B) (24K03249) from Japan Society for the Promotion of Science (to Y.M.),
386 Innovation Idea Contest from Tokyo Medical and Dental University (TMDU) (in 2022 to Y.M.
387 and in 2023 to Y.N.), Next Generation Researcher Training Unit from TMDU (to Y.M.) and
388 Priority Research Areas Grant from TMDU (to Y.M.), Research Grant from Uehara Memorial
389 Foundation (to Y.M.), Research Grant (Lifestyle-related diseases) from MSD Life Science
390 Foundation (to Y.M.), Medical Research Grant from Takeda Science Foundation (to Y.M.),
391 Academic Support from Bayer Yakuhin, Ltd. (to Y.M.), and Japan Agency for Medical Research
392 and Development (AMED) (24gm6910017h0001) (to E.S.).

393

394 **Author contributions**

YS performed the experiments, collected and analyzed data, developed experimental strategy and prepared the manuscript. MM supported the experiments. HM, WS and DT obtained the human kidney biopsy samples from patients. YS, YM, YN and MM established the hRPTECs and SM helped with the procedure. HK, FA, KS, TM, ES, and SU supported the data analysis. YW, SY, and YF resected the patients' kidneys as standard treatment for malignant diseases. YM supervised the project, modified experimental strategy and finalized the manuscript. All authors discussed the results and implications and provided comments on the manuscript.

404 **Figure Legends**

405 **Figure 1. A human kidney biopsy sample of a *Choleste-Help* nephropathy patient show renal**
406 **tubular injury and necrosis and surrounded interstitial fibrosis.**

407 **(a)** A HE staining on a human *Choleste-Help* nephropathy kidney. A scale bar: 200 μm.

408 **(b)** An immunostaining of KIM-1 and α-SMA on a *Choleste-Help* nephropathy kidney. Scale bars:
409 100 μm.

410

411 **Figure 2. Wild type mice showed acute kidney failure and Fanconi-like phenotype by**
412 ***Choleste-Help* toxic lot and puberulic acid.**

413 **(a)** Schematic overview of animal experiments treated with *Choleste-Help* toxic lot or puberulic
414 acid.

415 **(b)** Blood urea nitrogen (BUN), serum creatinine (Cr), urinary albumin (U-Alb), urinary glucose
416 (U-Glu) and urinary N-acetyl-β-D-glucosaminidase (U-NAG) of mice treated with PBS
417 control, *Choleste-Help* normal lot, toxic lot or puberulic acid (PA). n = 10 for control and for
418 *Choleste-Help* normal lot, n = 9 for toxic lot and n = 6 for puberulic acid.

419 **(c)** HE stainings on mouse kidneys of PBS control (vehicle), *Choleste-Help* normal lot, toxic lot
420 and pubeluric acid. Scale bars: 200 μm.

421 **(d)** Masson's Trichrome Stainings and statistical analysis of fibrotic areas on mouse kidneys PBS
422 control (vehicle), *Choleste-Help* normal lot, toxic lot (n = 8, 2 samples without kidney damage
423 excluded) and pubeluric acid. Scale bars: 200 μm.

424

425 **Figure 3. Mice treated with *Choleste-Help* toxic lot and puberulic acid exhibited highly**
426 **similar gene expression profiles, as revealed by RNA-seq analysis.**

(a) Principal component analysis (PCA) of RNA-seq samples. PCA was performed using rlog-transformed gene expression values. Each point represents one biological replicate. Samples are color-coded by treatment group: control (orange), normal lot (green), toxic lot (blue), and puberulic acid (magenta). PC1 and PC2 explain 86% and 4% of the total variance, respectively.

(b) Hierarchical clustering of RNA-seq samples. Samples were clustered based on Euclidean distance calculated from rlog-transformed gene expression values. Clustering was performed using complete linkage, and the resulting dendrogram illustrates the similarity of global transcriptomic profiles across the four treatment groups: control, normal lot, toxic lot, and puberulic acid. The x-axis labels represent individual biological replicates. Shorter branch lengths indicate greater similarity in expression profiles.

(c) Heatmap of the top 30 differentially expressed genes (DEGs) across treatment conditions. Row-scaled expression levels (Z-scores) of normalized RNA-seq counts are shown for the 30 most significant DEGs (padj < 0.05, $|\log2 \text{ fold change}| > 1$, baseMean > 10). Each row represents a gene, and each column corresponds to a biological replicate. Samples are annotated by treatment group: control (green), normal lot (blue), toxic lot (orange), and puberulic acid (magenta). Both genes and samples were hierarchically clustered using Euclidean distance and complete linkage. Color scale indicates standardized expression values (Z-scores), with red representing higher expression and blue representing lower expression relative to the mean of each gene.

(d) Volcano plot of differentially expressed genes between the toxic and normal lots. Each dot represents a gene, with red and blue indicating significantly upregulated and downregulated genes, respectively (adjusted p-value < 0.05 and $|\log2 \text{ fold change}| > 1$, baseMean > 10). Gray points represent genes with no significant change. The top 10 upregulated and downregulated

genes were labeled based on adjusted p-value ranking. For improved visualization, genes with extreme fold changes (|log2FC| > 10, n = 6) were excluded from the plot. The total number of significantly changed genes is indicated in the figure.

(e) Correlation of gene expression fold changes between treatment comparisons. Each point represents a gene, with its log2 fold change (log2FC) in normal lot vs toxic lot (x-axis) and puberulic acid vs control (y-axis). A Pearson correlation coefficient was 0.733. The red dashed line represents a linear regression fit.

(f) Venn diagram showing the overlap of differentially expressed genes (DEGs) between puberulic acid vs control and toxic lot vs normal lot. DEGs were defined by padj < 0.05, |log2FC| > 1, and baseMean > 10. A total of 4144 genes were shared between the two comparisons, accounting for 63.8% of the union set.

Figure 4. Mitochondrial function was significantly suppressed indicated by comprehensive transcriptomic analysis with RNA-seq

(a) GO Cellular Component (CC) enrichment analysis of differentially expressed genes. Dot plot showing the top 10 enriched GO terms (padj < 0.05). The x-axis represents Gene Ratio (number of input genes annotated in the term divided by the total number of input genes). The size of each dot reflects the gene count per GO term, and the color scale indicates the adjusted p-value.

(b) GO-Biological Process enrichment of downregulated genes. Dot plot showing the top 10 significantly enriched GO terms (padj < 0.05) among genes that were downregulated (log2FC < -1, baseMean > 10). The x-axis represents the Gene Ratio (the proportion of input genes associated with each term). The color gradient reflects the adjusted p-value (Benjamini-

472 Hochberg correction), where red indicates higher significance. Bubble size corresponds to the
473 number of genes enriched in each term.
474 **(c)** GO-Molecular Function enrichment of downregulated genes. Dot plot showing the top 10
475 significantly enriched molecular function (MF) terms (padj < 0.05) among genes
476 downregulated (log2FC < -1, baseMean > 10). The x-axis represents the Gene Ratio, defined
477 as the proportion of input genes annotated to each GO term. Dot size indicates the gene count,
478 while dot color represents the adjusted p-value. Long GO term names were wrapped to improve
479 readability, and the figure height was adjusted to prevent axis label overlap.
480
481 **Figure 5. Puberulic acid exhibited approximately half the cytotoxicity of cisplatin in**
482 **hRPTECs and a kidney injury marker and a DNA damage marker were upregulated**
483 **following puberulic acid exposure.**
484 **(a)** Cell viability of hRPTECs treated with puberulic acid or cisplatin. n = 7 for each condition
485 (performed 9 assays and excluded highest and lowest values as outliner). EC_{50} was estimated
486 using a 4-parameter logistic model (see Methods). Due to data sparsity at higher concentrations,
487 this value should be interpreted with caution.
488 **(b)** Representative western blotting images of γH2AX and Erk1/2 as a loading control from lysate
489 of puberulic acid-treated hRPTECs. Graphs represent densitometric values of each band
490 normalized to the corresponding internal control.
491 **(c)** Representative western blotting images of γH2AX, KIM-1 and Erk1/2 as a loading control
492 from lysate of puberulic acid-treated human kidney-derived tubuloids. Graphs represent
493 densitometric values of each band normalized to the corresponding internal control.
494

495 **Figure 6. Necrosis accounted for most of the cell death of hRPTECs treated with puberulic**
496 **acid.**
497 **(a)** Representative plots of flow cytometry on hRPTECs treated with puberulic acid or cisplatin
498 stained with Annexin V and propidium iodide (PI) as Annexin V assay. The graph shows the
499 fold change in early apoptosis (Annexin V positive, PI negative) and late apoptosis/necrosis
500 (Annexin V positive, PI positive), normalized to the control group. Independent experiments
501 were conducted three times for both the cisplatin group (n = 3) and the puberulic acid group (n
502 = 5). Statistical analyses were performed on raw (non-normalized) data, and the results were
503 reflected in the corresponding graphs.
504 **(b)** Representative plots of flow cytometry on hRPTECs treated with 100 μM puberulic acid
505 measuring time course of cell death. The graph shows the fold change in early apoptosis
506 (Annexin V positive, PI negative) and late apoptosis/necrosis (Annexin V positive, PI positive),
507 normalized to the control group. Independent experiments were performed twice for both the
508 24-hour group (n = 3) and the 40-hour group (n = 2). Statistical analyses were performed on
509 raw (non-normalized) data, and the results were reflected in the corresponding graphs.
510
511 **Figure 7. A decrease in mitochondrial membrane potential and ATP deficiency precede the**
512 **onset of cell death.**
513 **(a)** JC-1 staining of hRPTECs treated with puberulic acid and statistical analysis of red/green ratio.
514 Red color indicates J-aggregate and green color indicates JC-1 monomer. n = 18 in each
515 condition.

516 **(b)** ATP levels were measured and normalized to the respective control group at each time point.

517 The values at 0 h represent theoretical references. n = 6 for 6h, n=9 for 24h, and n = 3 for 48h.

518 statistical test: Kruskal–Wallis

519

References

1 Gabardi, S., Munz, K. & Ulbricht, C. A review of dietary supplement-induced renal dysfunction. *Clin J Am Soc Nephrol* **2**, 757-765 (2007). https://doi.org/10.2215/cjn.00500107

2 Knapik, J. J., Trone, D. W., Steelman, R. A., Farina, E. K. & Lieberman, H. R. Adverse effects associated with use of specific dietary supplements: The US Military Dietary Supplement Use Study. *Food Chem Toxicol* **161**, 112840 (2022). https://doi.org/10.1016/j.fct.2022.112840

3 LaW, M. o. H. *Information on Adverse Events associated with Beni-koji (Red Yeast Rice) related Products.*, <https://www.mhlw.go.jp/stf/seisakunitsuite/bunya/kenkou_iryou/shokuhin/daietto/index_00005.html> (2024).

4 Higa, Y. *et al.* Divergence of metabolites in three phylogenetically close Monascus species (M. pilosus, M. ruber, and M. purpureus) based on secondary metabolite biosynthetic gene clusters. *BMC Genomics* **21**, 679 (2020). https://doi.org/10.1186/s12864-020-06864-9

5 Fukami, H. *et al.* A Review of Red Yeast Rice, a Traditional Fermented Food in Japan and East Asia: Its Characteristic Ingredients and Application in the Maintenance and Improvement of Health in Lipid Metabolism and the Circulatory System. *Molecules* **26** (2021). https://doi.org/10.3390/molecules26061619

6 Maiguma, M. *et al.* Successful treatment of acute tubulointerstitial nephritis probably due to Benikoji CholesteHelp(®), a supplement containing red yeast rice. *CEN Case Rep* **14**, 24-28 (2025). https://doi.org/10.1007/s13730-024-00897-9

7 Maruyama, H. *et al.* Successful Resolution of Suspected Red Yeast Rice-induced Nephropathy. *Intern Med* (2025). https://doi.org/10.2169/internalmedicine.4908-24

8 Miyazaki, R. *et al.* Acute kidney tubular injury after ingestion of red yeast rice supplement. *Clin Kidney J* **17**, sfae151 (2024). https://doi.org/10.1093/ckj/sfae151

9 Shinzawa, M. *et al.* A nationwide questionnaire study evaluated kidney injury associated with Beni-koji tablets in Japan. *Kidney Int* **107**, 530-540 (2025). https://doi.org/10.1016/j.kint.2024.11.027

10 Tanaka, S. *et al.* Novel compounds isolated from health food products containing beni-koji (red yeast rice) with adverse event reports. *J Nat Med* **78**, 845-848 (2024). https://doi.org/10.1007/s11418-024-01827-w

553 11 Yoshinari, T. *et al.* Mechanism of puberulic acid contamination in red yeast rice tablets
554 that caused a serious food poisoning outbreak in Japan. *Proc Jpn Acad Ser B Phys Biol Sci*
555 (2025). https://doi.org/10.2183/pjab.101.017
556 12 Nakanoh, H. *et al.* Development and Validation of a Stem Cell–Based Kidney Organoid
557 Platform for Nephrotoxicity Assessment. *medRxiv*, 2025.2004.2030.651410 (2025).
558 https://doi.org/10.1101/2025.04.30.651410
559 13 Nakanoh, H. *et al.* in *Am J Nephrol* 1-9 (© 2025 The Author(s). Published by S.
560 Karger AG, Basel., 2025).
561 14 Iwatsuki, M. *et al.* In vitro and in vivo antimalarial activity of puberulic acid and its new
562 analogs, viticolins A-C, produced by Penicillium sp. FKI-4410. *J Antibiot (Tokyo)* **64**, 183-
563 188 (2011). https://doi.org/10.1038/ja.2010.124
564 15 Lukinich-Gruia, A. T. *et al.* Aristolochic acid I as an emerging biogenic contaminant
565 involved in chronic kidney diseases: A comprehensive review on exposure pathways,
566 environmental health issues and future challenges. *Chemosphere* **297**, 134111 (2022).
567 https://doi.org/10.1016/j.chemosphere.2022.134111
568 16 Cui, T. *et al.* Clinical and safety outcomes associated with aristolochic acid exposure: a
569 systematic review and meta-analysis. *Toxicol Mech Methods*, 1-11 (2025).
570 https://doi.org/10.1080/15376516.2025.2457340
571 17 Li, C. *et al.* Unveiling correlations between aristolochic acids and liver cancer:
572 spatiotemporal heterogeneity phenomenon. *Chin Med* **19**, 132 (2024).
573 https://doi.org/10.1186/s13020-024-01003-y
574 18 Ichimura, T. *et al.* Kidney injury molecule-1 is a phosphatidylserine receptor that confers
575 a phagocytic phenotype on epithelial cells. *The Journal of clinical investigation* **118**, 1657-
576 1668 (2008). https://doi.org/10.1172/jci34487
577 19 Mori, Y. *et al.* KIM-1 mediates fatty acid uptake by renal tubular cells to promote
578 progressive diabetic kidney disease. *Cell Metab* **33**, 1042-1061.e1047 (2021).
579 https://doi.org/10.1016/j.cmet.2021.04.004
580 20 Ichimura, T. *et al.* Kidney injury molecule-1 (KIM-1), a putative epithelial cell adhesion
581 molecule containing a novel immunoglobulin domain, is up-regulated in renal cells after
582 injury. *The Journal of biological chemistry* **273**, 4135-4142 (1998).
583 21 Yang, L., Besschetnova, T. Y., Brooks, C. R., Shah, J. V. & Bonventre, J. V. Epithelial cell
584 cycle arrest in G2/M mediates kidney fibrosis after injury. *Nat Med* **16**, 535-543, 531p
585 following 143 (2010). https://doi.org/10.1038/nm.2144

586 22 Ferenbach, D. A. & Bonventre, J. V. Mechanisms of maladaptive repair after AKI leading
587 to accelerated kidney ageing and CKD. *Nat Rev Nephrol* **11**, 264-276 (2015).
588 https://doi.org/10.1038/nrneph.2015.3
589 23 O'Sullivan, E. D., Hughes, J. & Ferenbach, D. A. Renal Aging: Causes and Consequences.
590 *J Am Soc Nephrol* **28**, 407-420 (2017). https://doi.org/10.1681/ASN.2015121308
591 24 Anders, H. J. & Schaefer, L. Beyond tissue injury-damage-associated molecular patterns,
592 toll-like receptors, and inflammasomes also drive regeneration and fibrosis. *J Am Soc*
593 *Nephrol* **25**, 1387-1400 (2014). https://doi.org/10.1681/ASN.2014010117
594 25 Zhang, Q. *et al.* Circulating mitochondrial DAMPs cause inflammatory responses to injury.
595 *Nature* **464**, 104-107 (2010). https://doi.org/10.1038/nature08780
596 26 Nicotera, P., Leist, M. & Ferrando-May, E. Intracellular ATP, a switch in the decision
597 between apoptosis and necrosis. *Toxicol Lett* **102-103**, 139-142 (1998).
598 https://doi.org/10.1016/s0378-4274(98)00298-7
599 27 Zubair, M. & Bokhari, S. R. A. in *StatPearls* (2025).
600 28 Leist, M., Single, B., Castoldi, A. F., Kuhnle, S. & Nicotera, P. Intracellular adenosine
601 triphosphate (ATP) concentration: a switch in the decision between apoptosis and necrosis.
602 *J Exp Med* **185**, 1481-1486 (1997). https://doi.org/10.1084/jem.185.8.1481
603 29 Eguchi, Y., Shimizu, S. & Tsujimoto, Y. Intracellular ATP levels determine cell death fate
604 by apoptosis or necrosis. *Cancer Res* **57**, 1835-1840 (1997).
605 30 Tsuchiya, K., Wang, W., Giebisch, G. & Welling, P. A. ATP is a coupling modulator of
606 parallel Na,K-ATPase-K-channel activity in the renal proximal tubule. *Proc Natl Acad Sci*
607 *U S A* **89**, 6418-6422 (1992). https://doi.org/10.1073/pnas.89.14.6418
608 31 Forst, A. L., Reichold, M., Kleta, R. & Warth, R. Distinct Mitochondrial Pathologies
609 Caused by Mutations of the Proximal Tubular Enzymes EHHADH and GATM. *Front*
610 *Physiol* **12**, 715485 (2021). https://doi.org/10.3389/fphys.2021.715485
611

a

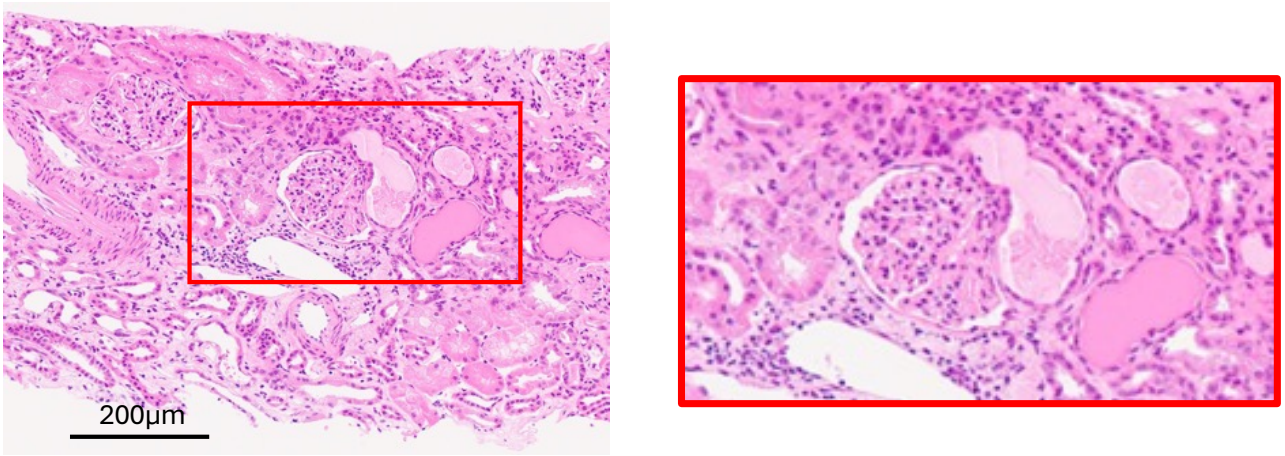

b

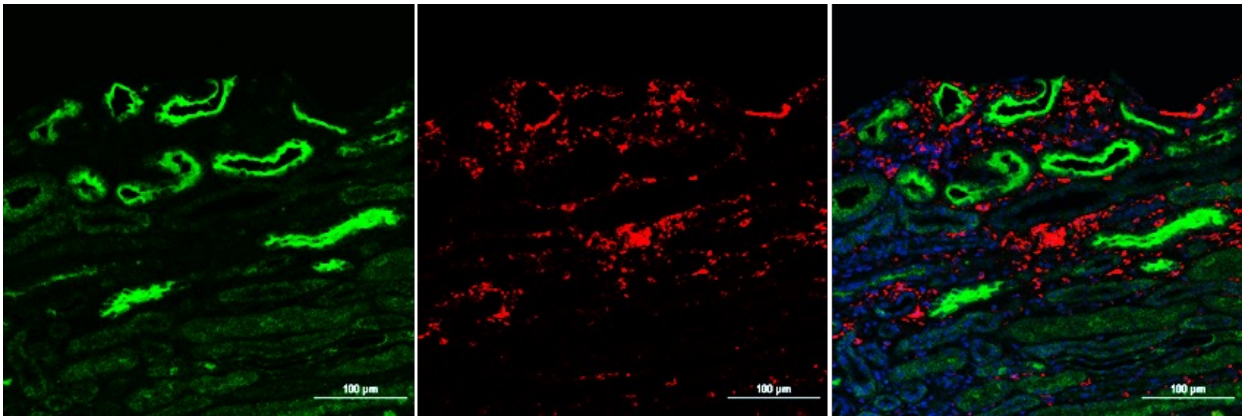

Figure 1

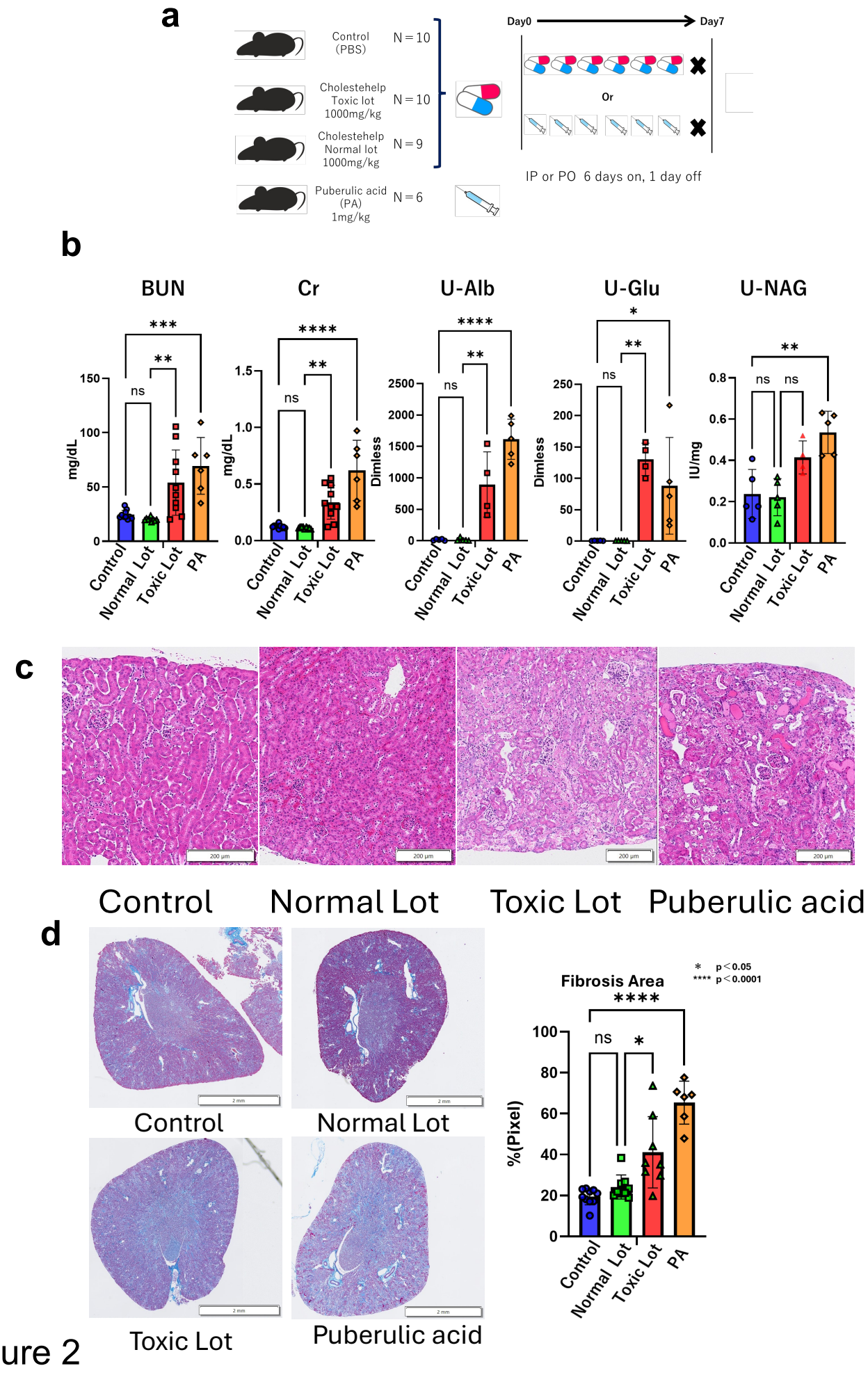
a
Control (PBS)
N = 10
Cholestehelp Toxic lot 1000mg/kg
N = 10
Cholestehelp Normal lot 1000mg/kg
N = 9
Puberulic acid (PA) 1mg/kg
N = 6
Day0
Day7
Or
IP or PO 6 days on, 1 day off
b
BUN
Cr
U-Alb
U-Glu
U-NAG
mg/dL
Dimless
IU/mg
ns
Control
Normal Lot
Toxic Lot
PA
c
Control
Normal Lot
Toxic Lot
Puberulic acid
d
Control
Normal Lot
Toxic Lot
Puberulic acid
Fibrosis Area
* p < 0.05
**** p < 0.0001
%(Pixel)

Figure 2

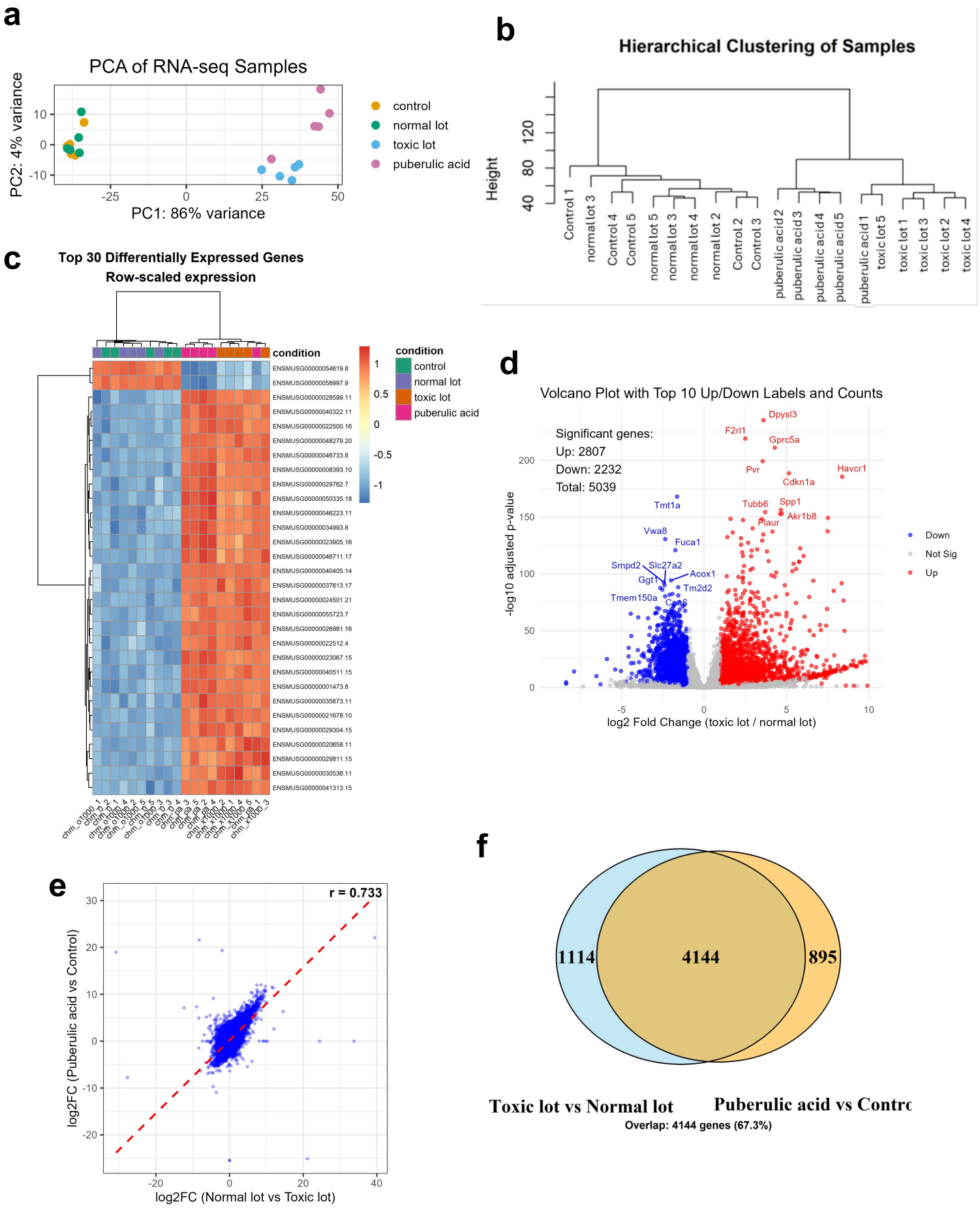
a
PCA of RNA-seq Samples
PC2: 4% variance
PC1: 86% variance
control
normal lot
toxic lot
puberulic acid
b
Hierarchical Clustering of Samples
Height
Control 1
normal lot 3
Control 4
Control 5
normal lot 5
normal lot 3
normal lot 4
normal lot 2
Control 2
Control 3
puberulic acid 2
puberulic acid 3
puberulic acid 4
puberulic acid 5
puberulic acid 1
toxic lot 5
toxic lot 1
toxic lot 3
toxic lot 2
toxic lot 4
c
Top 30 Differentially Expressed Genes
Row-scaled expression
condition
control
normal lot
toxic lot
puberulic acid
d
Volcano Plot with Top 10 Up/Down Labels and Counts
Significant genes:
Up: 2807
Down: 2232
Total: 5039
Dpysl3
F2rl1
Gprc5a
Pvr
Havcr1
Cdkn1a
Tmt1a
Tubb6
Spp1
Akr1b8
Plaur
Vwa8
Fuca1
Smpd2
Slc27a2
Acox1
Ggt1
Tm2d2
Tmem150a
Down
Not Sig
Up
-log10 adjusted p-value
log2 Fold Change (toxic lot / normal lot)
e
r = 0.733
log2FC (Puberulic acid vs Control)
log2FC (Normal lot vs Toxic lot)
f
1114
4144
895
Toxic lot vs Normal lot
Puberulic acid vs Contro
Overlap: 4144 genes (67.3%)

Figure 3

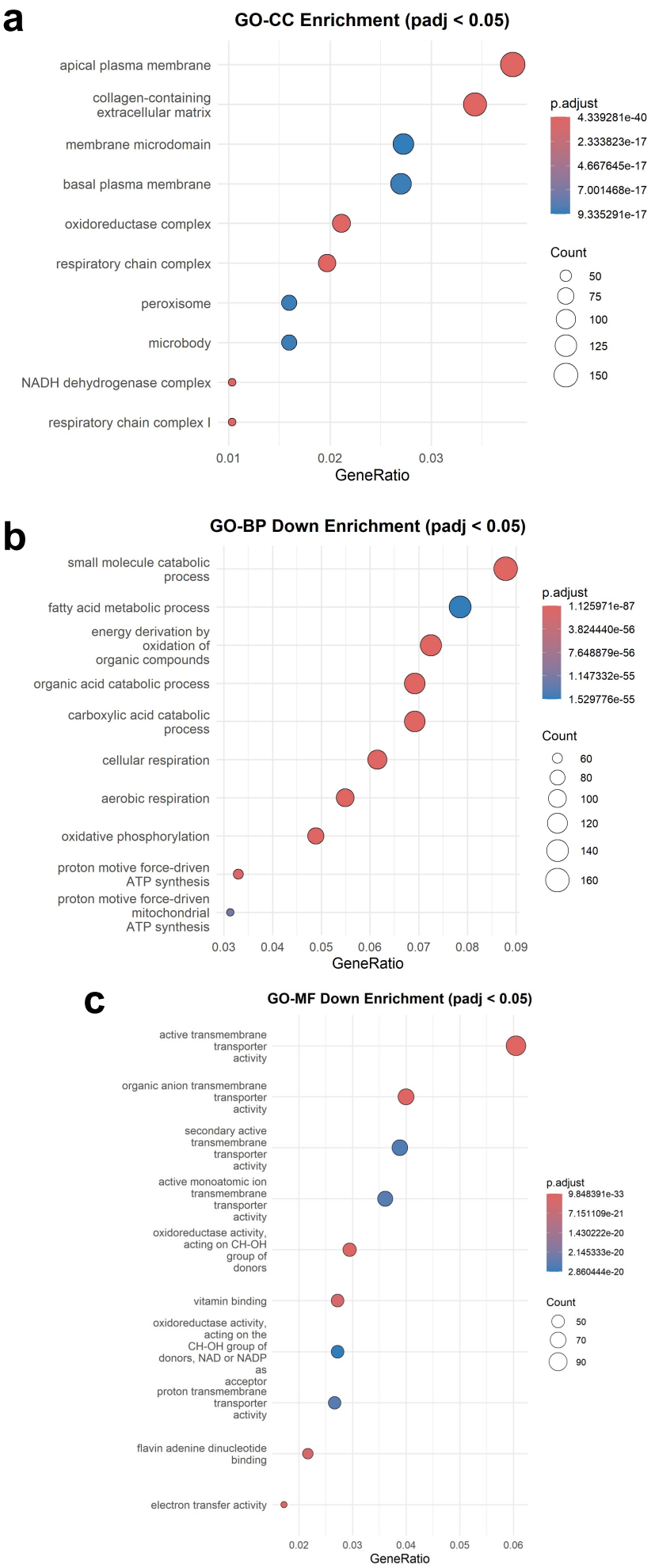
a
GO-CC Enrichment (padj < 0.05)
apical plasma membrane
collagen-containing extracellular matrix
membrane microdomain
basal plasma membrane
oxidoreductase complex
respiratory chain complex
peroxisome
microbody
NADH dehydrogenase complex
respiratory chain complex I
0.01
0.02
0.03
GeneRatio
p.adjust
4.339281e-40
2.333823e-17
4.667645e-17
7.001468e-17
9.335291e-17
Count
50
75
100
125
150
b
GO-BP Down Enrichment (padj < 0.05)
small molecule catabolic process
fatty acid metabolic process
energy derivation by oxidation of organic compounds
organic acid catabolic process
carboxylic acid catabolic process
cellular respiration
aerobic respiration
oxidative phosphorylation
proton motive force-driven ATP synthesis
proton motive force-driven mitochondrial ATP synthesis
0.03
0.04
0.05
0.06
0.07
0.08
0.09
GeneRatio
p.adjust
1.125971e-87
3.824440e-56
7.648879e-56
1.147332e-55
1.529776e-55
Count
60
80
100
120
140
160
c
GO-MF Down Enrichment (padj < 0.05)
active transmembrane transporter activity
organic anion transmembrane transporter activity
secondary active transmembrane transporter activity
active monoatomic ion transmembrane transporter activity
oxidoreductase activity, acting on CH-OH group of donors
vitamin binding
oxidoreductase activity, acting on the CH-OH group of donors, NAD or NADP as acceptor
proton transmembrane transporter activity
flavin adenine dinucleotide binding
electron transfer activity
0.02
0.03
0.04
0.05
0.06
GeneRatio
p.adjust
9.848391e-33
7.151109e-21
1.430222e-20
2.145333e-20
2.860444e-20
Count
50
70
90

Figure 4

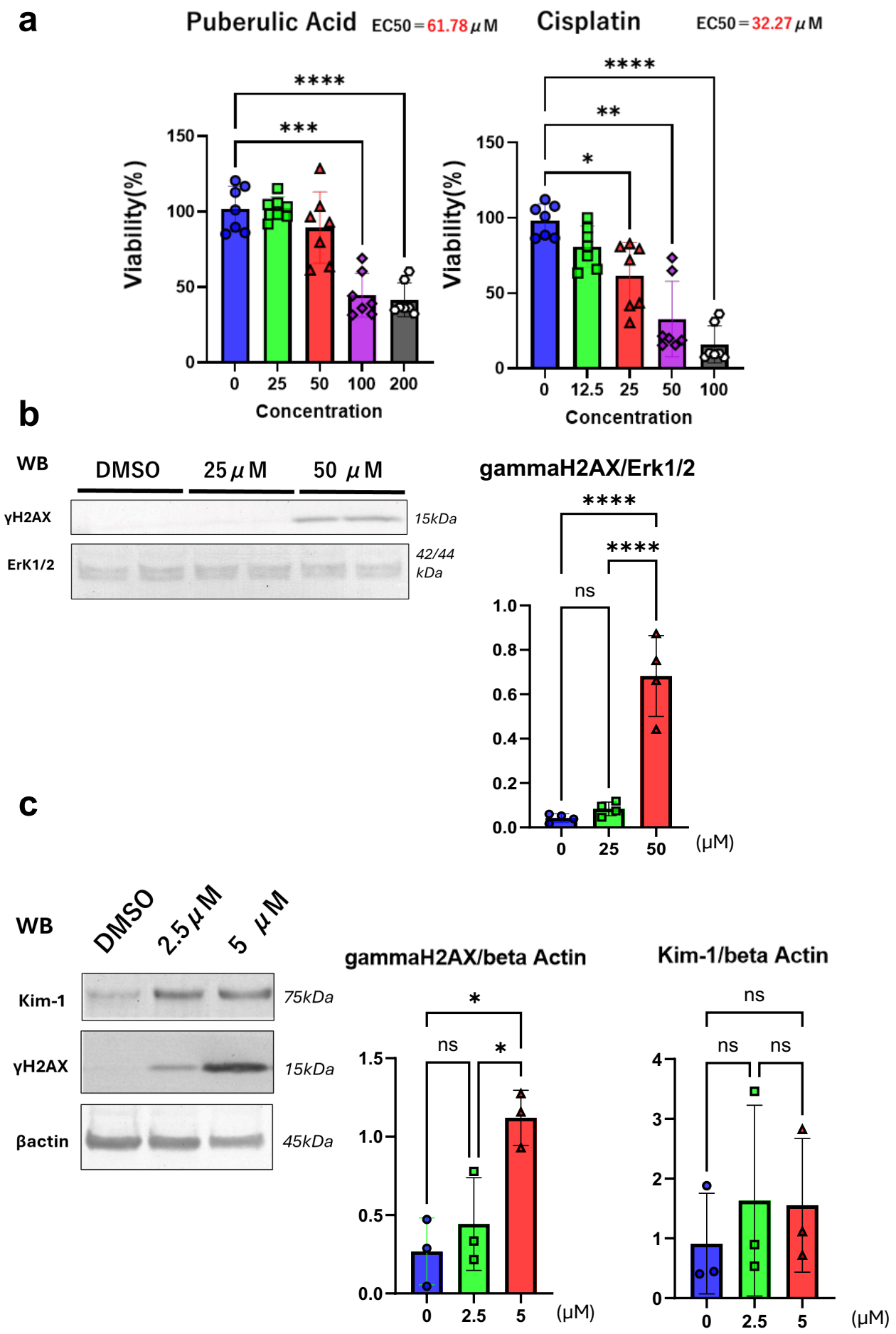
a
Puberulic Acid EC50=61.78μM
Cisplatin EC50=32.27μM
Viability(%)
Concentration
0 25 50 100 200
0 12.5 25 50 100
b
WB
DMSO
25μM
50 μM
γH2AX
ErK1/2
15kDa
42/44 kDa
gammaH2AX/Erk1/2
ns
(μM)
c
WB
DMSO
2.5μM
5 μM
Kim-1
γH2AX
βactin
75kDa
15kDa
45kDa
gammaH2AX/beta Actin
Kim-1/beta Actin
ns
(μM)

Figure 5

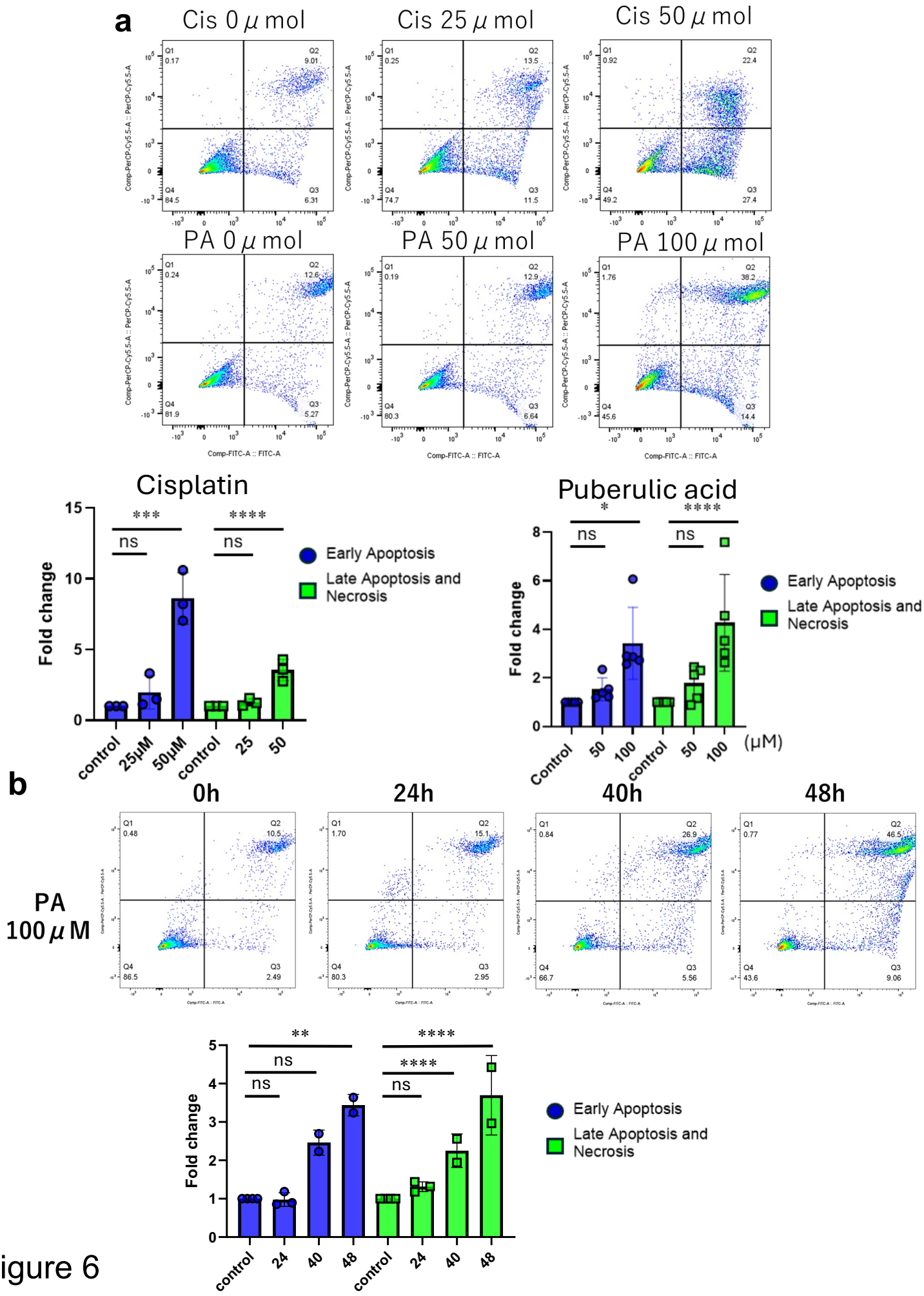
a
Cis 0 μ mol
Cis 25 μ mol
Cis 50 μ mol
PA 0 μ mol
PA 50 μ mol
PA 100 μ mol
Comp-PerCP-Cy5.5-A :: PerCP-Cy5.5-A
Comp-FITC-A :: FITC-A
Cisplatin
Puberulic acid
Fold change
Early Apoptosis
Late Apoptosis and Necrosis
control
25μM
50μM
25
50
100
(μM)
ns
***
****
*
b
PA 100 μ M
0h
24h
40h
48h
**
24
40
48

Figure 6

a

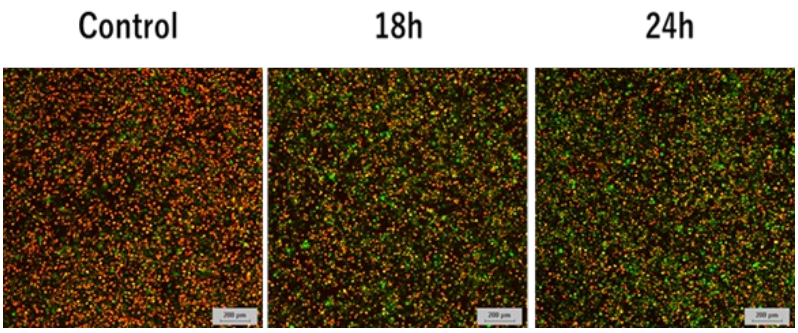
Control
18h
24h

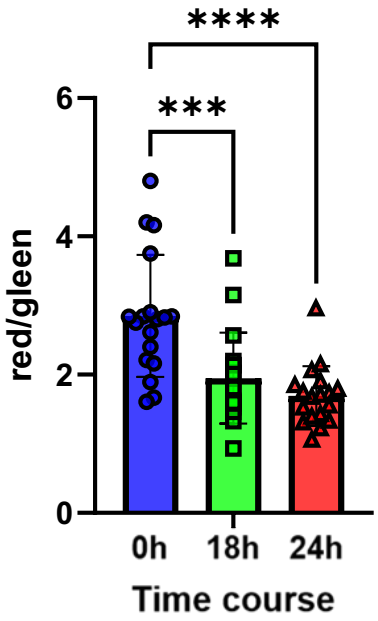
****
***
6
4
2
0
red/gleen
0h
18h
24h
Time course

b

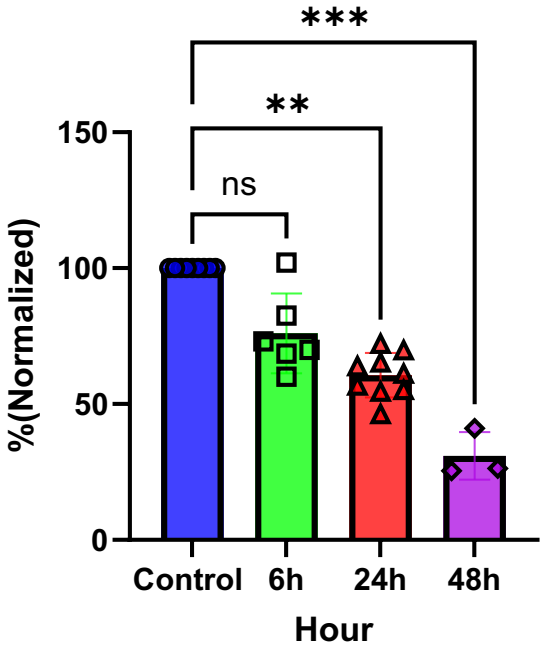
***
**
ns
150
100
50
0
%(Normalized)
Control
6h
24h
48h
Hour

Figure 7